

Temperature-induced collapse of spin dimensionality in magnetic metamaterials

Björn Erik Skovdal ^{*}, Nanny Strandqvist, Henry Stopfel , Merlin Pohlit, Tobias Warnatz, Samuel D. Sløetjes, Vassilios Kapaklis , and Björgvin Hjörvarsson 

Department of Physics and Astronomy, Uppsala University, Box 516, 751 20 Uppsala, Sweden



(Received 28 April 2021; revised 5 July 2021; accepted 13 July 2021; published 30 July 2021)

Spin and spatial dimensionalities are universal concepts, essential for describing both phase transitions and dynamics in magnetic materials. Lately, these ideas have been adopted to describe magnetic properties of metamaterials, replicating the properties of their atomic counterparts as well as exploring properties of ensembles of mesospins belonging to different universality classes. Here, we take the next step when investigating magnetic metamaterials not conforming to the conventional framework of continuous phase transitions. Instead of a continuous decrease in the moment with temperature, discrete steps are possible, resulting in a binary transition in the interactions of the elements. The transition is enabled by nucleation and annihilation of vortex cores, shifting topological charges between the interior and the edges of the elements. Consequently, the mesospins can be viewed as shifting their spin dimensionality, from 2 (XY-like) to 0 (vortices), at the transition. The results provide insight into how dynamics at different length scales couple, which can lead to thermally driven topological transitions in magnetic metamaterials.

DOI: [10.1103/PhysRevB.104.014434](https://doi.org/10.1103/PhysRevB.104.014434)

I. INTRODUCTION

Magnetic metamaterials [1] composed of mesospins as building blocks [2] offer the possibility of tailoring magnetic interactions and dynamics in almost arbitrary ways. Previous investigations have mainly been focused on the collective magnetic order, dynamics, and more exotic aspects such as frustration of artificial spin systems [1,3–5], while the internal magnetization and dynamics of the mesospins are less explored [6–8]. For instance, extensive efforts have been made to mimic magnetic systems of various spatial and spin dimensionalities, where the shapes of the elements have been used to enforce mesospins to be Ising- or XY-like [2,9–13]. Even systems consisting of *both* Ising and XY mesospins have been fabricated and investigated, which is a testament to the versatility of metamaterials [14,15]. The common denominator in all these investigations is that the spin dimensionality is treated as a static property. Yet, the mesospins offer access to continuous degrees of freedom and rich internal magnetic states that go well beyond their atomic analogues. This attribute is the focal point of the present study, as we turn our attention to arrays of mesospins that can exhibit two distinct magnetization states: collinear and vortex spin textures [16,17]. The mesospins can be thought of as having variable spin dimensionality, where the interaction strength depends on

the inner magnetic textures. It is therefore possible to couple the changes in spin dimensionality to changes in the collective properties of the mesospins. The coupling of these internal and external degrees of freedom, in combination with the exploration of the role of topological effects on the observed transitions [18,19], is therefore the main motivation behind this work.

II. MATERIALS AND METHODS

A. Sample manufacturing

Two sets of samples were prepared: one set for photoemission electron microscopy (PEEM) studies employing x-ray magnetic circular dichroism (XMCD) and the other set for magneto-optical Kerr effect (MOKE) measurements. The samples were prepared depositing elemental Fe (99.95 at. %) and Pd (99.95 at. %) in an ultrahigh-vacuum (base pressure below $\sim 2 \times 10^{-7}$ Pa) DC magnetron sputtering system, operating using high-purity argon gas (99.995%). The following sample structure was used: fused silica/Pd [40 nm]/Fe₁₃Pd₈₇ [10 nm]/Pd [2 nm] [20]. By using FePd, the ordering temperature and the spin dimensionality of the parent material can be chosen by the distribution and concentration of Fe, independently of film thickness [21,22]. After growth, electron beam lithography (EBL) was used to pattern the Fe₁₃Pd₈₇ layers into circular islands arranged on square lattices (see Fig. 1). The Ar⁺-ion milling process, following development of the EBL resist and subsequent mask deposition, was stopped prior to penetration through the Pd seed layer, providing this way electrical continuity across the whole sample surface. The PEEM-XMCD samples with a disk diameter of $D = [75, 150, 350]$ nm were fabricated having two inter-disk distances: one with the nearest-neighbor distance set to

^{*}bjorn_erik.skovdal@physics.uu.se

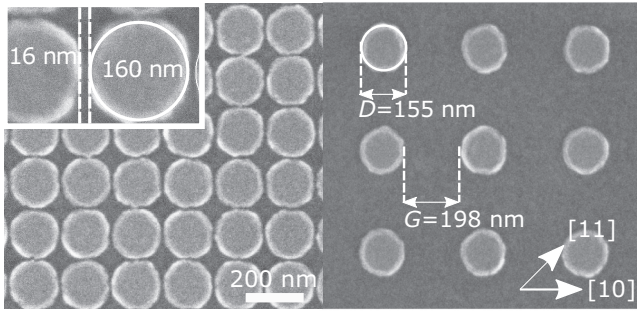


FIG. 1. The magnetic metamaterial—square arrays of circular islands. Scanning electron microscopy image of a representative structure with disks of a diameter $D = 150$ nm. Left: Interacting disks with a gap of $G = 20$ nm. The inset shows the same structure at a higher magnification. Right: Noninteracting disks with $G = D + 40$ nm. The major symmetry axes of the patterned square lattices, [10] and [11], are also denoted.

$G = D + 40$ nm, rendering the interdisk coupling sufficiently weak to be ignored, and the other with an edge-to-edge gap of $G = 20$ nm to enable interactions between the magnetic elements [23]. The MOKE samples were patterned into disks with a diameter of $D = [250, 350, 450]$ nm with a small edge-to-edge gap of $G = 20$ nm.

B. PEEM-XMCD

To determine the magnetic state of the noninteracting and strongly coupled disks, photoemission electron microscopy and strongly coupled disks, photoemission electron microscopy, employing x-ray magnetic circular dichroism (PEEM-XMCD), was performed at the HERMES beamline at the SOLEIL synchrotron [24], and the 11.0.1 beamline at the Advanced Light Source [25]. Prior to imaging, the samples were cooled from room temperature to roughly 100 K, in absence of any external magnetic field. The energy of the synchrotron beam was tuned to the Fe L_3 edge (708.4 eV), and magnetic contrast was obtained from the asymmetry ratio of intensities between right- and left-handed circularly polarized synchrotron radiation.

C. Micromagnetic simulations and topological considerations

To understand the role of the interactions, we chose to explore the energies of the vortex and collinear state for different disk sizes, using the MuMax³ micromagnetic simulation software [26]. The simulations, used to mimic the experimental conditions, were performed using one single disk, as well as square arrays of disks ($G = 20$ nm), with periodic boundary conditions. The saturation magnetization, $M_{\text{sat}} = 3.5 \times 10^5$ A/m, and exchange stiffness, $A_{\text{ex}} = 3.36 \times 10^{-12}$ J/m, were chosen based on previous work by Östman *et al.* [20] and Ciuciulkaite *et al.* [27]. The in-plane cell size was set to $0.50(1)l_{\text{ex}}$, where l_{ex} is the exchange length as defined by M_{sat} and A_{ex} [26].

D. Hysteresis protocols

The magnetization data were collected using a MOKE system in longitudinal configuration with the sample mounted on a cryostat, in a temperature range of $80 \text{ K} < T < 400 \text{ K}$.

The p -polarized incident laser beam with $\lambda = 659$ nm had a Gaussian profile with a spot diameter of roughly 2 mm. The number of islands contributing to the signal are therefore on the order of 10^7 . The reflected laser beam was passed through an analyzer (extinction ratio of $1 : 10^5$) and then captured using a Si biased detector, connected to a pre-amplifier and lock-in amplifier. In addition, the lock-in amplifier was used to modulate the incident laser beam using a Faraday cell. The sinusoidal external magnetic field applied along [10] of the square lattice (see Fig. 1) had an amplitude of 40 mT and a frequency of 0.11 Hz unless otherwise stated. The magnetization data in all figures have been binned (3 : 1) for aesthetic purposes.

III. RESULTS AND DISCUSSION

We begin by discussing the size dependence of internal spin textures and spontaneous magnetic order in circular islands. To this end, we fabricated samples with nominal disk diameters $D = [75, 150, 350]$ nm, having edge-to-edge gaps $G = [20, D + 40]$ nm, on one and the same wafer. This approach allows us to disregard any uncertainty related to, e.g., composition and thickness of the islands. Representative parts of the samples with 150 nm islands are illustrated in Fig. 1. The results of photoemission electron microscopy on these samples, with magnetic contrast obtained by using x-ray magnetic circular dichroism (PEEM-XMCD), are displayed in Fig. 2. As inferred by the black and white contrast, the disks with a diameter of 75 nm are all found to exhibit a collinear component for both small and large distances between the islands. Similarly, the 350 nm islands are found to be in a vortex state for both the short and long distance between the islands, with no preferred sense of rotation. When the disk diameter is 150 nm, a vortex state is obtained when the distance between the islands is large, while a substantial number of mesospins have a collinear component, when the distance between the islands is 20 nm. Thus, for this particular diameter of islands, the interaction appears to be strong enough to influence the inner magnetic states. To understand the role of the interactions and the interplay between the involved length scales, we need to have a look at the energy landscape of the magnetic textures.

The magnetic energy of the metamaterial can be expressed as $E = E_t + E_s + E_j$, where E_t is the energy cost of the magnetic texture arising from exchange interactions within the islands, E_s is the magnetostatic energy, and E_j is the energy associated with the magnetostatic coupling between the islands. By calculating the energy as a function of the vortex core displacement d for a disk with radius R , a single path—out of many—in the energy landscape separating the collinear and the vortex state can be obtained. Ding *et al.* used the same reasoning when calculating the energy barrier separating the two states in a single Co dot analytically [28]. Here, we chose to do it numerically as the calculations can be generalized to include interactions of elements in an arbitrary array. The results obtained from calculations of interacting ($G = 20$ nm) and noninteracting ($G = D + 40$ nm) disks with $D = [75, 150, 350]$ nm are shown in Fig. 3. When a vortex core is at the center of an island, its displacement is defined to be zero and the energy is $E \approx E_t$ because $E_s \approx E_j \approx 0$.

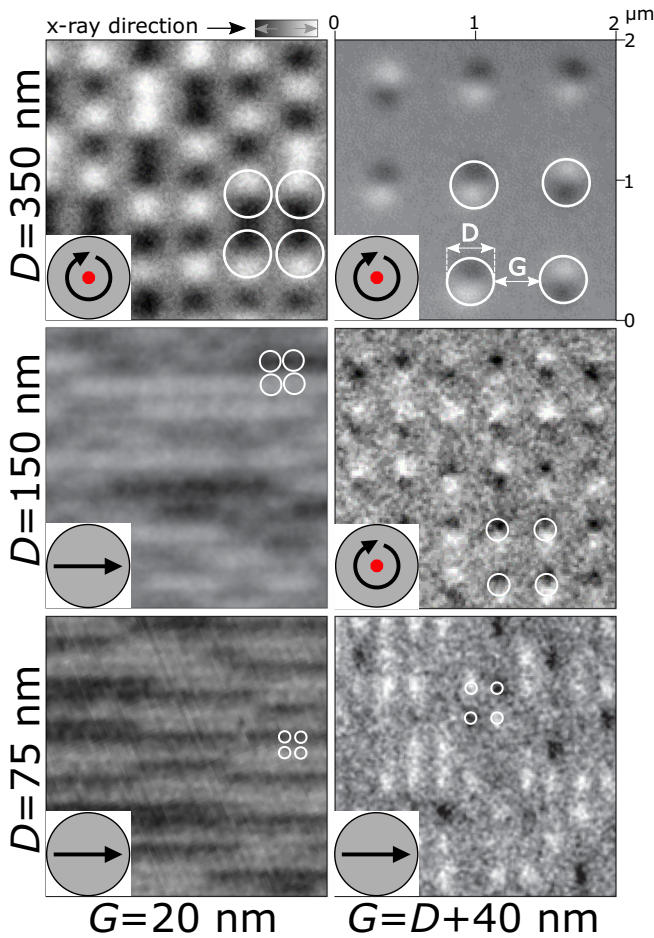


FIG. 2. Diameter and interaction dependence of the disk magnetic texture. PEEM-XMCD images of interacting islands (left column), and noninteracting islands (right column), recorded at approximately 100 K after cooling from room temperature in absence of external fields. Disks with a diameter of 350 nm have a preferred vortex texture for both interacting and noninteracting disks, while disks with 75 nm diameter end up in the collinear state in both cases. Disks with a diameter of 150 nm, display a stabilization of the collinear state when the distance between the islands is small, while otherwise exhibiting vortex textures. The white circles indicate the disk sizes and positions, obtained by overlapping the PEEM-x-ray absorption spectroscopy images.

Shifting the core from the center gives rise to a collinear component, and consequently a stray field with a corresponding magnetostatic energy. For the purpose of the calculation, the (virtual) vortex core can even be moved outside the disk ($d > R$), corresponding to a C state (see Fig. 3), with varying degree of gradients in the magnetic texture. The energy maxima obtained at $d \approx 0.9R$ can be viewed as activation barriers separating the vortex and the collinear states. The energy difference between the interacting and noninteracting islands increases with increasing d , highlighted by the shaded areas in the figure. The activation barrier separating the collinear from the vortex state is also affected by changes in G .

In these simulations we use the energies obtained by MuMax³'s built-in functions for the vortex and the collinear state, without allowing for relaxation of the magnetization

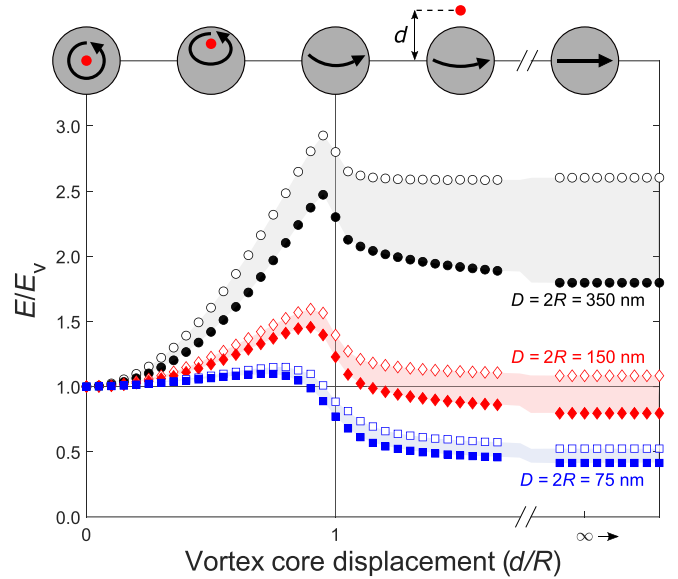


FIG. 3. The energy landscape of the transition between the vortex and the collinear state. The landscape was obtained numerically by gradually moving the vortex core outward from the center of the disks. Filled symbols represent the energy of interacting disks ($G = 20$ nm), while empty symbols for noninteracting disks ($G = \infty$). The shaded areas represent the magnetostatic coupling E_j . The energies plotted are normalized to the total energy of the vortex state E_v . The energy barrier between the two states can be chosen by the selection of the diameter and the distance between the islands. The top part shows a schematic of the states for different values of d , where the red dot indicates the position of the vortex core; when $d > R$, a C state is obtained.

with respect to the total energy. Using this approach, the intermediate states can be calculated without the systems collapsing into either the vortex or the collinear state, enabling us to estimate the height of the activation barrier. Qualitatively, the same results can be obtained in relaxed systems by moving the core by means of an applied magnetic field. This approach, however, does not provide any information on the potential in the vicinity of the maximum of the activation barrier. In the simulations with interacting islands, all vortex cores were displaced such that the collinear component of each island was along [10], mimicking the influence of an applied field along [10] as in the MOKE experiments. The choice of either uniform or alternating vortex chirality had a negligible impact on the outcome of the simulations.

The size dependence in the energy of interacting and noninteracting mesospins is summarized in Fig. 4. For noninteracting islands the collinear state has the lowest energy when $D \lesssim 140$ nm, while a vortex state is favored when the diameter is larger. With an inter-island distance of 20 nm, a collinear state is favored up to about $D \approx 190$ nm. Consequently the critical size at which the vortex state is favored is shifted to larger diameters when interactions become prominent. Hence, a region of bistability (marked by a gray shading in the figure) is obtained. We have thereby rationalized the results displayed in Fig. 2, i.e., why the 150 nm islands form vortices in absence of interactions, while a significant amount of the mesospins show a collinear component when

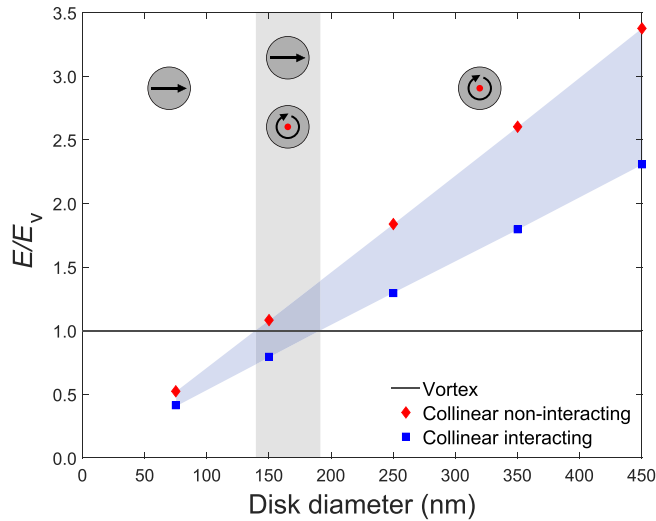


FIG. 4. The boundary between vortex and collinear states. The energy of the collinear state is lowered (blue squares) by inter-island interactions. As a result, it is possible to stabilize collinear states for a range of diameters which otherwise favor formation of vortices (gray shaded area). The energies plotted are normalized to the total energy of the vortex state E_v .

they interact. When collinear, the mesospins can be viewed as being two-dimensional [14] (XY-rotor) and zero-dimensional [20] when in a vortex state. At the same time, the magnetic texture can be defined in terms of topological quasiparticles (see Appendix A) [29,30]. The states can thereby be defined as having topological charge of $+1$, determined by $1 - g$, with g being the genus of the structure [19]. The boundary of the islands can host magnetic charges with fractional winding numbers, w , which together with the winding number of the bulk charge, q , must add up to 1 (see Appendix A) [19,31]. Consequently, the winding of the vortex can be seen as being transferred to the edge of the island when the magnetization changes from a vortex to a collinear state ($d > R$). The transition from a vortex to a collinear state therefore involves no change in the total winding number, while the magnetic cores and their polarity annihilate at the edges of the islands.

While it is trivial to annihilate vortices by applying an external field, the opposite is certainly not true. For this reason we chose to focus on the field and temperature dependence of islands with a diameter of 250 nm and larger ($D = [250, 350, 450]$ nm), with gaps $G = 20$ nm. Disks in this size range spontaneously form vortices when cooled, while the application of an external magnetic field results in a collinear state, allowing us to control the magnetic texture of the mesospins. The stability of the *dressed* collinear state can thus be investigated by removing the external field while monitoring the magnetization of the samples. Representative magnetization loops for the 450 nm islands, recorded at four different temperatures, are provided in the top half of Fig. 5. The bottom part illustrates the temperature dependence of the magnetization.

At $T = 275$ K the hysteresis loops display a typical vortex nucleation (H_n) and annihilation (H_a) signature with zero remanence [32], in line with both the PEEM-XMCD results as

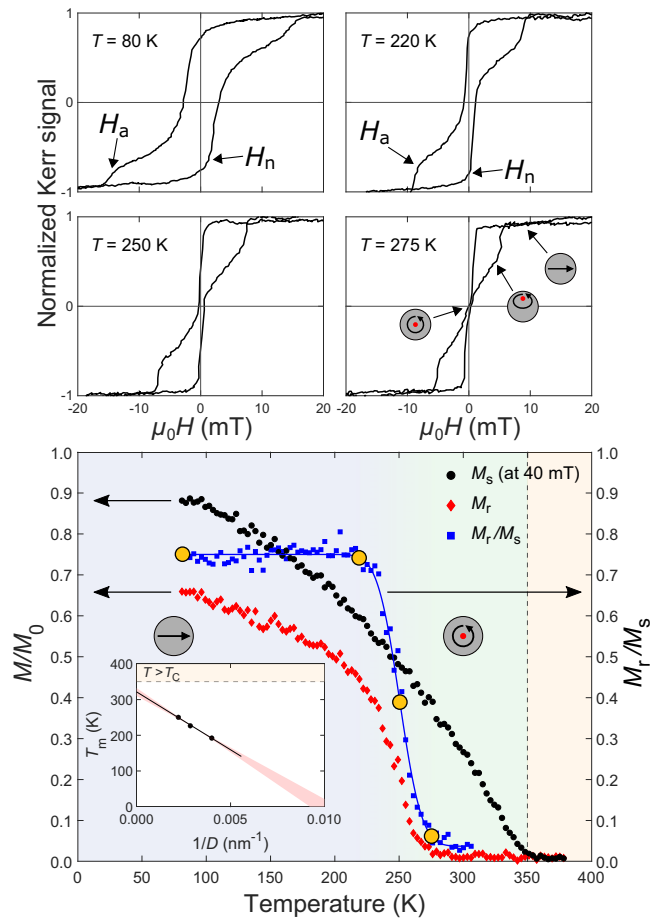


FIG. 5. Temperature dependence of the dimensionality transition in a magnetic metamaterial. Magnetization measurements with the applied field along [10] (see Fig. 1) for the 450 nm islands having a gap of $G = 20$ nm. Top: Representative hysteresis curves at 80, 220, 250, and 275 K. The curves have been normalized for each individual temperature. The nucleation field crosses $\mu_0 H = 0$ at approximately 220 K, indicating a stability of the collinear state below this temperature, during the timescale of the measurement. Bottom: The magnetization as a function of temperature at 0 and 40 mT as well as the ratio $M_m = M_r/M_s$. The orange filled circles mark the temperatures at which the hysteresis curves, shown above, were taken. The size dependence of the transition temperature, T_m , for island sizes $D = [250, 350, 450]$ nm is shown in the inset. The error bars of the data in the inset are smaller than the data point symbols. The uncertainty in the extrapolated values (one standard deviation) is symbolized by the red shading in the inset.

well as the simulations. At temperatures below ≈ 250 K, the sample exhibits clear remanence, consistent with the presence of a ferromagnetic state. Ferromagnetic response requires alignment of mesospins with a net moment, in stark contrast to the zero-field PEEM-XMCD results. The reduction of the remanent magnetization (M_r) with temperature contains both the decrease of the moment of the material (intrinsic material properties) as well as changes in the texture and orientation of the mesospins. To disentangle these contributions we need to identify their signatures. Changes in the material-related magnetization can be described by a power law up to the ordering temperature of the materials (T_C), while the temperature de-

pendence of the texture and orientation of the mesospins is unknown. However, separation of the two contributions can be obtained by identifying the difference in their field dependence. For instance, it is sufficient to apply a relatively weak field to remove most of the magnetic texture within a disk, while weak fields only marginally affect the thermally induced excitations of the magnetization in the material. This is seen in the field dependence displayed in Fig. 5: at $T = 275$ K, a field of approximately 6 mT is sufficient for obtaining a transition from a vortex to a collinear state. Nevertheless, this field does little to alter the thermally induced reduction of the magnetization. We can therefore consider the magnetization at a field of 40 mT as predominantly representative for the material; i.e., we define this magnetization as the saturation of the mesoscopic texture (M_s). Consequently, the temperature dependence of $M_m = M_r/M_s$ can be thought of as corresponding to the temperature dependence of the remanence of the mesospin texture.

The results displayed in the bottom half of Fig. 5 (450 nm islands) illustrate M_r , M_s , and $M_m = M_r/M_s$, the inferred remanence of the mesospins. A plateau with $M_m = 3/4$ is observed, consistent with constant magnetic texture and thereby a fixed topology of the mesospins, below 220 K. At the same time, a substantial fraction of the moment (1/4) is perpendicular and/or antiparallel with respect to the direction of the net magnetization. At 220 K there is an abrupt change in M_m , which vanishes at 270 K. From 270 K and up to the intrinsic Curie temperature of the material, the obtained hysteresis loops are consistent with the presence of vortex states. Thus, we observe a sharp transition from a collective state of interacting mesospins to noninteracting vortex states of the elements with zero net magnetization. To this observation we assign a change from a state with a spin dimensionality of 2 to a state with zero spin dimensionality. This result should be compared with previous findings of Östman *et al.* where no remanence was observed even at temperatures as low as 5 K, for islands of the same size and similar material composition, but with $G = 50$ nm [20]. This highlights the impact of distance between the islands (G) on the interaction energy and its effect on the lifetime of the metastable collinear state.

The temperature dependence of this transition can be determined by fitting an error function to the data, from which the temperature T_m where $M_m(T_m) = \frac{1}{2}M_m(T = 0 \text{ K})$ (inset of Fig. 5, bottom panel) is determined. An error function was chosen without assigning any physical interpretation to it. A clear size dependence is observed, which follows a $T_m \propto 1 - 1/D$ relationship. The results imply an increased stability of the metastable collinear state with increasing disk size. This is interpreted as a result of stronger interactions between larger islands, which stabilize the metastable collinear state by an increase in the activation barrier. Extrapolation to infinite size yields a transition temperature just below T_C of the continuous film, which is reassuring as T_C must be the upper limit of T_m , regardless of island size. As the value of T_m also depends on the sweep frequency, f , of the magnetic field (see Appendix B) and should depend strongly on G , the apparently linear relationship may be coincidental. Extrapolation to zero in T_m yields ≈ 100 nm island size, which can be understood as the lower limit for obtaining the transition. However, as illustrated in Fig. 4, the collinear state is already favored when

$D \lesssim 190$ nm, rendering this region unattainable. As the vortex state is energetically favored above this size, the observed transitions in 250, 350, and 450 nm elements are kinetically limited and do not correspond to thermodynamic phase transitions in a strict sense. This is further emphasized by the observed frequency dependence of the transition temperature, T_m (see Appendix B). The dressed mesospins (collinear state) in this size range are therefore in an arrested metastable state with the boundaries of the mesospins being vital for the creation and annihilation process of the vortex cores.

IV. CONCLUSIONS

The temperature dependence of the topologically homeomorphic transition is not only defined by the material properties and size of the mesospins but also by their mutual interactions and internal degrees of freedom. In particular, the distance between the elements alters the inter-island interactions and thereby the internal magnetic states, while at the same time, the internal magnetic states affect the interactions and thereby the magnetic order. The interplay between these two length scales leads to an exotic transition, which is to say that it is not based on thermally induced randomization. Rather, the transition pertains to a thermally activated change within the elements, resulting in a collapse of the effective interaction strength and the mesospin dimensionality. The transition discussed here does not have any trivial classical counterpart, calling for a new conceptual framework involving mutual dependence of energy and length scales [33]. The results represent stumbling steps toward understanding emergent properties and complexity that may extend beyond the immediate field of physics [34,35].

The data that support the findings of this study are available from the authors upon reasonable request.

ACKNOWLEDGMENTS

The authors would like to acknowledge the excellent user support provided to them at the Advanced Light Source (Dr. Andreas Scholl, Dr. Rajesh Chopdekar) and SOLEIL (Dr. Rahid Belkhou) synchrotrons, as well as Dr. Erik Östman for helping out with data collection. This research used resources of the Advanced Light Source, a US DOE Office of Science User Facility under Contract No. DE-AC02-05CH11231. The excellent support and infrastructure of the MyFab facility at the Ångström Laboratory of Uppsala University are also highly appreciated. B.H. acknowledges financial support from the Swedish Research Council (Project No. 2019-05379). V.K. acknowledges support from the Knut and Alice Wallenberg Foundation project “Harnessing light and spins through plasmons at the nanoscale” (2015.0060) and the Swedish Research Council (Project No. 2019-03581).

APPENDIX A: MESOSPIN CLASSIFICATION

Figure 6 illustrates the vortex and the collinear states, as well as their corresponding topological charges residing in the bulk and on the edges, respectively. A transition between the two states is topologically allowed for elements of finite size,

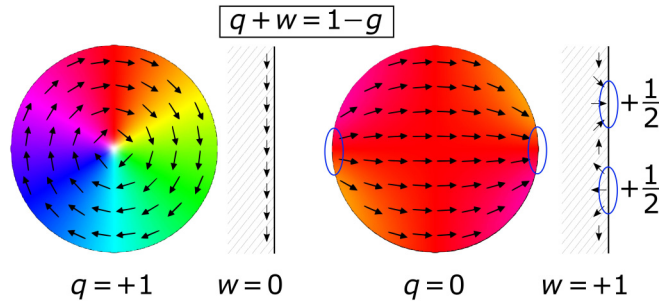


FIG. 6. Magnetic texture and topology of a vortex (left) and a collinear state (right). There is substantial texture in the magnetic state referred to as collinear; however, the net transverse moment is zero. The interior topological charge $q = +1$ (vortex) can be transferred to two topological charges, with $w = +\frac{1}{2}$, at the edges (collinear) [19]. The schematics next to the textures depict the changes in the direction of the magnetization with respect to the edge and the resulting winding number.

and can be driven by applying external fields or thermally induced fluctuations [20]. The amount of topological charge that can be residing in an element is determined by the genus g (number of holes) of the structure, providing an additional knob for the design of texture topology in magnetic metamaterials. This transition is followed by a change in the effective spin dimensionality of the mesospins, which is 0 for the vortex and 2 for the collinear state (see also Table I). Note that in the interior of the mesospins, noninteger winding numbers cannot exist [19,29]. This is not the case though for the edges where half-integer winding numbers are possible and thus topological charges, w , which further correlate to stray field emanating from or into the mesospin [19]. These appear in pairs, resulting in integer numbers for the total charge on the edge.

The spin dimensionality d relates to the behavior of the effective mesospin moment, which for planar mesospins can be 0, 1, or 2 dimensional [2,14,16], as illustrated in Table I. The sense of rotation c describes the circulation (clockwise and anticlockwise) of the magnetic texture and acquires nonzero values in the vortex case (0-dimensional mesospin) [36]. The polarity p relates to the direction of the out-of-plane component (up or down) of the magnetization for the core in a vortex. Finally, when considering the planar topology, the bulk topological charge q defines the magnetic texture of the mesospins,

TABLE I. Classification scheme for the planar mesospins.

Mesospin type			
Mesospin property	Vortex	Ising	XY-rotor
Dimensionality, d	0	1	2
Sense of rotation, c	± 1	0	0
Polarity, p	± 1	0	0
Bulk topological charge, q	+1	0	0
Edge topological charge, w	0	$+\frac{1}{2}, +\frac{1}{2}$	$+\frac{1}{2}, +\frac{1}{2}$

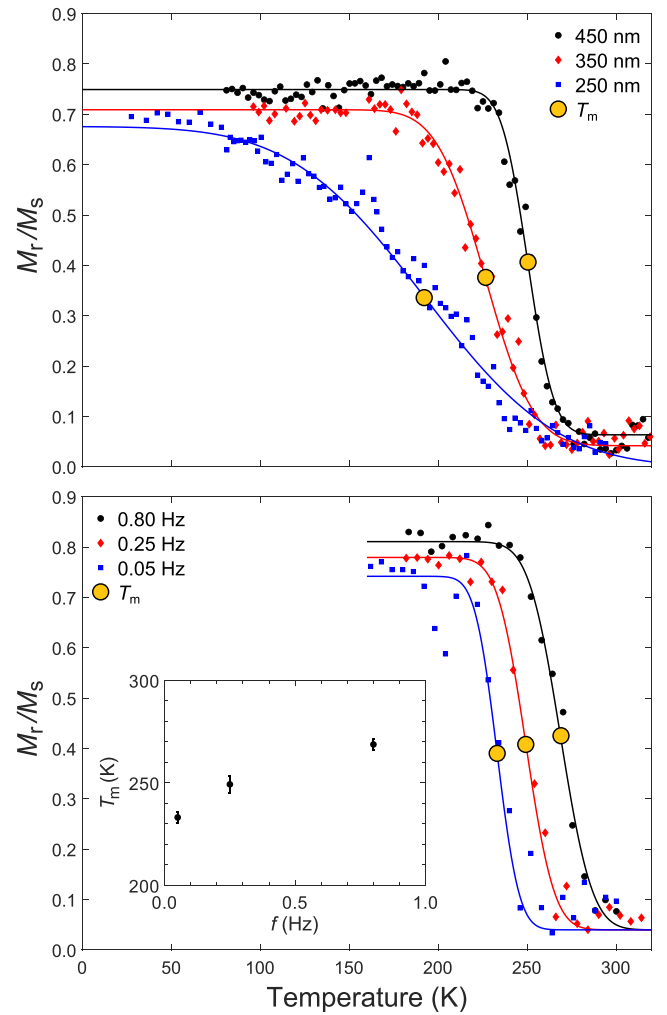


FIG. 7. Size and frequency dependence of the dimensionality transition. Top: Temperature dependence of the remanent versus the in-field (40 mT) magnetization ratio, for all available disk diameters and for a gap $G = 20$ nm. The values of T_m , determined from the inflection points of the fitted curves, versus the reciprocal of the disk diameter D , is found in the inset of Fig. 5. Bottom: The frequency dependence of the transition for a disk diameter $D = 450$ nm and gap $G = 20$ nm. A monotonic shift to higher temperature with increasing frequency is observed, compatible with thermally activated relaxation processes of magnetic metamaterial. The orange filled circles in each panel mark the extracted temperatures presented in the respective insets.

being +1 for vortex states and 0 for Ising or XY-rotor states. The blue colored cells refer to mesospin properties and their associated transitions, particularly studied in this work.

APPENDIX B: KINETICS

The observed size dependence (upper panel of Fig. 7) can be compared with results of Ding *et al.*, where the relaxation time of noninteracting Co dots was found to rapidly decrease with increasing dot size at a given temperature [28]. This is quite the opposite of our findings presented here,

leading us to conclude that it is the interactions of larger islands that lead to an increased collinear stability, rather than a direct dependence on D . With this in mind, we can understand our observed size dependence. For larger islands, more thermal energy is required to break the bonds between the collinear islands; however, as soon as a few islands do transition into the vortex state, their neighbors suddenly have fewer collinear neighbors with which to interact. This initiates an avalanche effect, where the entire lattice collapses into the vortex state over a narrow range of temperatures. Since larger islands without collinear neighbors have faster relaxation times, the transition becomes sharper for larger islands. This is also seen in our simulations (Fig. 3), where the difference in activation barrier height (from the collinear to the vortex state) between islands with $G = 20$ and $G = \infty$ is larger for larger islands. This further emphasizes the drastic relaxation expected for larger islands as soon as the transition has been activated. The largest observed size dependence of the different curves is therefore the temperature at which the transition is activated (when M_r/M_s begins to deviate from the

plateau), as well as its broadness. The temperature at which M_r/M_s has reached zero only varies marginally between the samples.

To obtain a better understanding on the interplay between kinetics and thermodynamics, we explored the frequency dependence, f , of the applied field on the remanent magnetization. The dwell time at zero field provides a time window for a relaxation, which is proportional to the inverse scanning frequency. The findings are illustrated in the lower panel of Fig. 7, depicting a clear frequency dependence of the response from the 450 nm disks. Increasing the scanning frequency results in an increase of the transition temperatures (inset in Fig. 7, lower panel), illustrating the impact of the kinetic limitations on the transition [8,37]. Consequently, we conclude that the ferromagnetic component observed at low temperatures corresponds to a metastable arrested state. The frequency dependence cannot be captured by a single exponential, highlighting the non-Arrhenius behavior of the homeomorphic transition. We are not aware of any models that can capture the observed behavior.

-
- [1] L. J. Heyderman and R. L. Stamps, *J. Phys.: Condens. Matter* **25**, 363201 (2013).
- [2] E. Östman, U. B. Arnalds, V. Kapaklis, A. Taroni, and B. Hjörvarsson, *J. Phys.: Condens. Matter* **30**, 365301 (2018).
- [3] C. Nisoli, R. Moessner, and P. Schiffer, *Rev. Mod. Phys.* **85**, 1473 (2013).
- [4] C. Nisoli, V. Kapaklis, and P. Schiffer, *Nat. Phys.* **13**, 200 (2017).
- [5] N. Rougemaille and B. Canals, *Eur. Phys. J. B* **92**, 62 (2019).
- [6] S. Gliga, A. Kákay, R. Hertel, and O. G. Heinonen, *Phys. Rev. Lett.* **110**, 117205 (2013).
- [7] S. Gliga, A. Kákay, L. J. Heyderman, R. Hertel, and O. G. Heinonen, *Phys. Rev. B* **92**, 060413(R) (2015).
- [8] S. D. Slöetjes, B. Hjörvarsson, and V. Kapaklis, *Appl. Phys. Lett.* **118**, 142407 (2021).
- [9] O. Sendetskiy, V. Scagnoli, N. Leo, L. Anghinolfi, A. Alberca, J. Lüning, U. Staub, P. M. Derlet, and L. J. Heyderman, *Phys. Rev. B* **99**, 214430 (2019).
- [10] M. Ewerlin, D. Demirbas, F. Brüßing, O. Petravic, A. A. Ünal, S. Valencia, F. Kronast, and H. Zabel, *Phys. Rev. Lett.* **110**, 177209 (2013).
- [11] R. Streubel, N. Kent, S. Dhuey, A. Scholl, S. Kevan, and P. Fischer, *Nano Lett.* **18**, 7428 (2018).
- [12] N. Leo, S. Hohenstein, D. Schildknecht, O. Sendetskiy, H. Luetkens, P. M. Derlet, V. Scagnoli, D. Lançon, J. R. L. Mardegan, T. Prokscha, A. Suter, Z. Salman, S. Lee, and L. J. Heyderman, *Nat. Commun.* **9**, 2850 (2018).
- [13] U. B. Arnalds, J. Chico, H. Stopfel, V. Kapaklis, O. Bärenbold, M. A. Verschuuren, U. Wolff, V. Neu, A. Bergman, and B. Hjörvarsson, *New J. Phys.* **18**, 023008 (2016).
- [14] U. B. Arnalds, M. Ahlberg, M. S. Brewer, V. Kapaklis, E. T. Papaioannou, M. Karimipour, P. Korelis, A. Stein, S. Ólafsson, T. P. A. Hase, and B. Hjörvarsson, *Appl. Phys. Lett.* **105**, 042409 (2014).
- [15] E. Östman, H. Stopfel, I.-A. Chioar, U. B. Arnalds, A. Stein, V. Kapaklis, and B. Hjörvarsson, *Nat. Phys.* **14**, 375 (2018).
- [16] T. Shinjo, *Science* **289**, 930 (2000).
- [17] M. Kläui, C. A. F. Vaz, L. Lopez-Diaz, and J. A. C. Bland, *J. Phys.: Condens. Matter* **15**, R985 (2003).
- [18] N. D. Mermin, *Rev. Mod. Phys.* **51**, 591 (1979).
- [19] O. Tchernyshyov and G.-W. Chern, *Phys. Rev. Lett.* **95**, 197204 (2005).
- [20] E. Östman, U. B. Arnalds, E. Melander, V. Kapaklis, G. K. Pálsson, A. Y. Saw, M. A. Verschuuren, F. Kronast, E. T. Papaioannou, C. S. Fadley, and B. Hjörvarsson, *New J. Phys.* **16**, 053002 (2014).
- [21] M. Pärnaste, M. Marcellini, E. Holmström, N. Bock, J. Fransson, O. Eriksson, and B. Hjörvarsson, *J. Phys.: Condens. Matter* **19**, 246213 (2007).
- [22] T. P. A. Hase, M. S. Brewer, U. B. Arnalds, M. Ahlberg, V. Kapaklis, M. Björck, L. Bouchenoire, P. Thompson, D. Haskel, Y. Choi, J. Lang, C. Sánchez-Hanke, and B. Hjörvarsson, *Phys. Rev. B* **90**, 104403 (2014).
- [23] K. Y. Guslienko, V. Novosad, Y. Otani, H. Shima, and K. Fukamichi, *Phys. Rev. B* **65**, 024414 (2001).
- [24] R. Belkhou, S. Stanescu, S. Swaraj, A. Besson, M. Ledoux, M. Hajlaoui, and D. Dalle, *J. Synchrotron Radiat.* **22**, 968 (2015).
- [25] A. Doran, M. Church, T. Miller, G. Morrison, A. T. Young, and A. Scholl, *J. Electron Spectrosc. Relat. Phenom.* **185**, 340 (2012).
- [26] A. Vansteenkiste, J. Leliaert, M. Dvornik, M. Helsen, F. Garcia-Sanchez, and B. Van Waeyenberge, *AIP Adv.* **4**, 107133 (2014).
- [27] A. Ciuciulkaite, E. Östman, R. Brucas, A. Kumar, M. A. Verschuuren, P. Svedlindh, B. Hjörvarsson, and V. Kapaklis, *Phys. Rev. B* **99**, 184415 (2019).
- [28] H. F. Ding, A. K. Schmid, D. Li, K. Y. Guslienko, and S. D. Bader, *Phys. Rev. Lett.* **94**, 157202 (2005).

- [29] S. Zhang, A. A. Baker, S. Komineas, and T. Hesjedal, *Sci. Rep.* **5**, 15773 (2015).
- [30] C. Donnelly, K. L. Metlov, V. Scagnoli, M. Guizar-Sicairos, M. Holler, N. S. Bingham, J. Raabe, L. J. Heyderman, N. R. Cooper, and S. Gliga, *Nat. Phys.* **17**, 316 (2021).
- [31] S. D. Slöetjes, E. Folven, and J. K. Grepstad, *Phys. Rev. B* **101**, 014450 (2020).
- [32] R. P. Cowburn, D. K. Koltsov, A. O. Adeyeye, M. E. Welland, and D. M. Tricker, *Phys. Rev. Lett.* **83**, 1042 (1999).
- [33] K. G. Wilson, *Sci. Am.* **241**, 158 (1979).
- [34] C. Castellano, S. Fortunato, and V. Loreto, *Rev. Mod. Phys.* **81**, 591 (2009).
- [35] J. Michaud and A. Szilva, *Phys. Rev. E* **97**, 062313 (2018).
- [36] A. S. Jenkins, E. Grimaldi, P. Bortolotti, R. Lebrun, H. Kubota, K. Yakushiji, A. Fukushima, G. de Loubens, O. Klein, S. Yuasa, and V. Cros, *Appl. Phys. Lett.* **105**, 172403 (2014).
- [37] M. Pohlit, G. Muscas, I.-A. Chioar, H. Stopfel, A. Ciuciulkaite, E. Östman, S. D. Pappas, A. Stein, B. Hjörvarsson, P. E. Jönsson, and V. Kapaklis, *Phys. Rev. B* **101**, 134404 (2020).